Research on Engineering Structures & Materials
www.jresm.org
Research Group

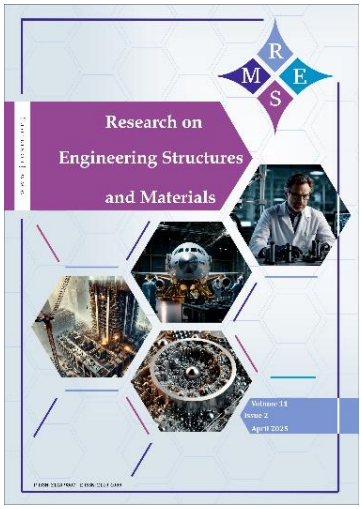

Pulse-type interference suppression based on an improved wavelet threshold for wideband partial discharge detection in transformers

Guanghu Xu, Qingchuan Zhang, Gang Chen, Zhongqiang Zhan, Dandong He

Online Publication Date: 10 September 2026

URL: http://www.jresm.org/archive/resm2026-1950vk0721rs.html
DOI: http://dx.doi.org/10.17515/resm2026-1950vk0721rs

Journal Abbreviation: *Res. Eng. Struct. Mater.*

To cite this article
Xu G, Zhang Q, Chen G, Zhan Z, He D. Pulse-type interference suppression based on an improved wavelet threshold for wideband partial discharge detection in transformers. *Res. Eng. Struct. Mater.*, 2026; 12(5): 4193-4209.

Disclaimer
All the opinions and statements expressed in the papers are on the responsibility of author(s) and are not to be regarded as those of the journal of Research on Engineering Structures and Materials (RESM) organization or related parties. The publishers make no warranty, explicit or implied, or make any representation with respect to the contents of any article will be complete or accurate or up to date. The accuracy of any instructions, equations, or other information should be independently verified. The publisher and related parties shall not be liable for any loss, actions, claims, proceedings, demand or costs or damages whatsoever or howsoever caused arising directly or indirectly in connection with use of the information given in the journal or related means.

Published articles are freely available to users under the terms of Creative Commons Attribution - NonCommercial 4.0 International Public License, as currently displayed at here (the "CC BY - NC").

Research on Engineering Structures & Materials
www.jresm.org
Research Group

Research Article

Pulse-type interference suppression based on an improved wavelet threshold for wideband partial discharge detection in transformers

Guanghu Xu [*,1,2,a], Qingchuan Zhang [1,2,b], Gang Chen [1,2,c], Zhongqiang Zhan [1,2,d], Dandong He [1,2,e]

[1]*Xinjiang Key Laboratory of Extreme Environment Operation and Testing Technology for Power Transmission & Transformation Equipment, Urumqi, China*
[2]*State Grid Xinjiang Electric Power Company Electric Power Research Institute, Urumqi, China*

Article Info

Article History:

Received 21 July 2026
Accepted 31 Aug 2026

Keywords:

Partial discharge;
Improved wavelet threshold;
Pulse-type interference suppression;
Power transformers;
High-frequency current transformer (HFCT);
Denoising

Abstract

Pulse-type interference at high-voltage (HV) and ultra-high voltage (UHV) transformer sites severely limits the effectiveness of partial discharge (PD) detection, as conventional pulse current measurement below 1 MHz leaves 12-pulse ripple, corona, and electronic switching pulses overlapping with genuine PD signals in both time and frequency domains. This work develops an improved wavelet threshold method tightly integrated with a wideband detection platform featuring a 150 kHz to 60 MHz signal conditioning bandwidth coupled with a 3–50 MHz high-frequency current transformer (HFCT) sensor. A continuously differentiable threshold function with adjustable factor α is constructed to bridge hard and soft thresholding, a layer-dependent adaptive estimator replaces the universal threshold to match noise variance at each decomposition level, and a time-frequency cumulative energy function performs pulse pre-localization before discrimination. Validation on 500 simulation samples, 320 laboratory records from a 220 kV physical platform, and 180 field signals from three substations shows an average SNR gain of 9.3 dB, combined fitness F of 2.38 at 5 dB input SNR (F is a figure of merit balancing noise suppression and waveform preservation), and laboratory identification rates of 95.2%, 93.6%, and 94.3% for the three interference categories. Pooled field detection accuracy reaches 93.7%, feature-parameter recovery errors stay within 8.1%, and single-record processing settles at 52 ms. Pilot deployments reduced the detection blind zone from 6%–8% down to 2.5%–3%. These findings demonstrate the practical value of the proposed method for improving the reliability of online insulation condition assessment in harsh substation environments.

© 2026 MIM Research Group. All rights reserved.

1. Introduction

High voltage and extra high voltage transformers represent essential elements in the conversion and transmission of electrical energy on a large scale. According to CIGRE figures, about 58.8% of all defects in HVDC systems are transformer-based problems, and insulation failure accounts for almost 50% of such incidents [36]. The phenomenon of partial discharge (PD) is an early warning sign as well as a catalyst in causing insulation breakdown, making PD detection a necessary pre-requisite for effective health status analysis [1]. It is hence mandatory that continuous online monitoring be conducted with sensor networks installed in bushings, windings, and tap changers [2]. Various reviews on the technique of electrical diagnosis have categorized IEC 60270 pulse

*Corresponding author: guanghuXu123@hotmail.com
[a]orcid.org/0009-0002-7761-7984; [b]orcid.org/0009-0000-8701-8673; [c]orcid.org/0009-0000-4207-0670; [d]orcid.org/0009-0009-1758-4915; [e]orcid.org/0009-0004-3042-6106
DOI: http://dx.doi.org/10.17515/resm2026-1950vk0721rs

current testing, ultra-high frequency testing, and acoustic emission techniques as complementary methods, with each being limited by sensitivity and bandwidth requirements [3]. Electrical and acoustic sensing are physically complementary: the HFCT channel preserves the nanosecond-scale waveform needed to discriminate PD from pulse-type interference, whereas acoustic emission mainly supports spatial localization. The present study validates the electrical (HFCT) chain only; acoustic-electric fusion on the same platform is treated as future work (Section 4.4). UHV grids operating under extreme environmental conditions, such as those in Northwest China where on the order of one hundred large transformers are commissioned every year, require rigorous pre-energization PD testing, because a defect that escapes factory or site acceptance testing can readily develop into failure once the unit is energized.

The field PD measurements faces three consistent difficulties. Firstly, the harsh electromagnetic background of substation environments which includes rich harmonics, periodic oscillations, and white noise, with a noise floor sometimes drowning out the square-wave calibration signal when high load is applied. Secondly, bandwidth limitations under conventional standards restrict the measurement. As described in the IEC 60270 and GB/T 7354 pulse current measurement method, the frequency range of the test falls below 1 MHz, resulting in a loss of the rising edge at the nanosecond level of PD pulses. The research on UHF measurements revealed that the real PD signal spectrum reaches frequencies higher than 100 MHz; hence, band-limited sampling loses valuable information necessary to differentiate the signal from noise [4]. Finally, calibrating wideband receivers under practical conditions is difficult, which requires the replication of the impulse waveform and its frequency by means of the charge injection calibrator [5]. Pulse-type interference brings another level of challenge. The twelve-pulse ripple associated with converter operations is present with a period of 1.67 ms, corona pulses occur around the 90° and 270° phases, while electronic switching generates spindle pulses at 120° intervals. All three types of pulses behave like actual PD signals in traditional time domain analysis [6]. Effective differentiation relies on feature-based separation, not amplitude alone [7].

Five years of research have yielded multiple denoising pathways, each with its own unique attributes and drawbacks. The wavelet thresholding method continues to be the standard technique utilized, and the maximum overlap discrete wavelet transform technique has reconstructed severely noisy PD pulses from cables, but fixed thresholding continues to add a persistent bias term to the remaining coefficients [8]. The soft thresholding method creates a bias term intentionally, whereas the hard thresholding method creates discontinuous points at the threshold value, which results in pseudo-Gibbs oscillations once the signal is reconstructed. Empirical mode decomposition has been implemented on the PD pulses, but mode mixing and end effect problems affect the initial part of the signal [9]. Parameter optimized variational mode decomposition has exhibited improved separation of narrowband interferers[10], while the Aquila optimizer combination of VMD with K-SVD [11] along with whale-VMD combined with adaptive filtering and wavelet denoising [12] produce improved SNR but entail iterative searching. Hybrid SVD-VMD systems have improved rejection of white noise but involve intensive computation especially for long signal records [13]. Normalized spectral kurtosis-based spectrum segmentation approaches have been tried out in multiple source environments [14], while algorithms for periodic narrow band interference have proved selective interference cancellation capability without making the PD waveform flat [15]. Acoustic-VMD-CNN-LSTM [16], deep residual shrinkage network [17], and CNN-BiLSTM with attention [18] based recognition algorithms have attained impressive accuracies on laboratory data. The primary challenge remains achieving an optimal trade-off between waveform accuracy and computational delay under field conditions with pulse-like interference: iterative decompositions and deep recognizers require per-record latencies of several hundred milliseconds to seconds when executed on embedded hardware (for the baselines re-implemented in this work, 185 ms for adaptive SVD and 420 ms for EMD-based thresholding on a 1024-sample record, Section 3.4), which is incompatible with sub-100 ms online updating.

The following three proposals are offered as solutions to the aforementioned deficiencies. The first proposal is a continuously differential threshold function involving a parameter α varying in the interval (0, 1). This threshold function combines the benefits of hard thresholding and soft thresholding without the pseudo-Gibbs effect of the former while lowering the bias of the latter.

The second suggestion is a threshold estimation scheme dependent on the layer, where the noise standard deviation σj for each decomposition layer is estimated based on the median of the detail coefficients so that higher frequency layers have larger thresholds than lower frequency layers. The third part is related to the incorporation of the proposed algorithm into a wideband detection platform utilizing a signal conditioning bandwidth of 150 kHz to 60 MHz coupled with a 3–50 MHz HFCT sensor, where a time-frequency cumulative energy approach enables pulse localization before classification. The rest of the paper is structured as follows. Section 2 describes the hardware platform, interference, algorithm, and evaluation methodology. Section 3 includes simulation, laboratory and field experiments together with comparative performance analysis. Section 4 analyzes stability, adaptation, computational cost, and constraints. Section 5 concludes the work.

2. Materials and Methods

2.1 Wideband Partial Discharge Detection Hardware Platform

The HFCT detector employs a split-core (openable) nanocrystalline toroid with an initial relative permeability of 3×10^4 and a maximum relative permeability of 4×10^5, and with dimensions R_1 = 60 mm (inner radius), R_2 = 80 mm (outer radius), and d = 15 mm (height). The two half-cores are hinged and spring-clamped, so that the sensor can be fitted around the bushing-tap lead or the tank grounding conductor of an in-service or newly commissioned transformer without disconnecting the grounding circuit. The detecting coil employs 24 turns of 0.6 mm enameled copper wires equally distributed with half turns on each side of the core material. The toroid coil is placed inside an aluminum alloy shielding case with an internal spacing of 2 mm which avoids shorting but preserves its shielding capability. The HFCT has been characterized experimentally for its −3 dB operational range from 3 MHz to 50 MHz, which therefore defines the effective measurement band of the complete chain, and its transfer impedance exceeds the 5 mV/mA required by State Grid corporate standards, analogous to the existing designs of HFCT used for oil-based partial discharge calibration tests [19].

The signal conditioning process operates from 150 kHz to 60 MHz, with a noise level measured less than 0.5 mV. The conditioning band is deliberately wider than the HFCT passband: its 150 kHz lower edge is retained so that the same front end can be calibrated against the IEC 60270 pulse-current path and can characterize the 12-pulse ripple spectrum (Section 2.2), whereas the effective PD measurement band of the whole chain is set by the HFCT (3–50 MHz). Below 3 MHz the HFCT response rolls off at roughly 20 dB/decade, so the 100 kHz ripple component is attenuated by about 30 dB; however, because the ripple amplitude at the bushing tap is two to three orders of magnitude larger than that of PD pulses and its thyristor commutation edges contain harmonic content extending into the MHz range, residual ripple and commutation transients still reach the ADC at amplitudes comparable to PD. Algorithmic suppression of this residual, rather than reliance on the sensor roll-off alone, is therefore required. The analog-to-digital conversion process operates at 250 MSps, recreating the PD events in which their rise times are in the range of ns to tens of ns. Further processing operations are performed using a heterogeneous multi-core processor operating at 1.6 GHz, with 2 GB DDR4 and 16 GB eMMC memory; this processor executes the implementation used for all laboratory and field results in Section 3, whereas the FPGA+DSP figures quoted in Section 4.3 stem from a separate synthesis study of a future embedded port. Synchronization in measurement nodes is done using GPS and Beidou discipline with ns accuracy.

The calibration procedure consists of three steps regarding the cutoff frequency, sensitivity, and pulse calibrator responses. The center frequency of the passband is determined by the geometric mean relationship $f_c = \sqrt{f_H f_L}$, where f_H and f_L are defined as the upper and lower 3 dB points from the practical front end. The calibration of apparent charge is performed using an impulse generator that provides the output loop resistance of detection impedance ranging from 50 Ω to 200 Ω. The apparent charge q (pC) reported in Section 3 is obtained from the peak HFCT output voltage V_p (mV) through the calibrator-derived scale factor $q = k_q V_p$, where k_q (pC/mV) is determined by injecting known charges with the impulse generator into the same detection loop before each test; the waveforms in Fig. 5 are shown in mV, and the pC values quoted in the text follow from this

calibration. The entire physical structure of the system includes the HFCT, conditioner, ADC, and digital backend, as illustrated in Fig. 1.

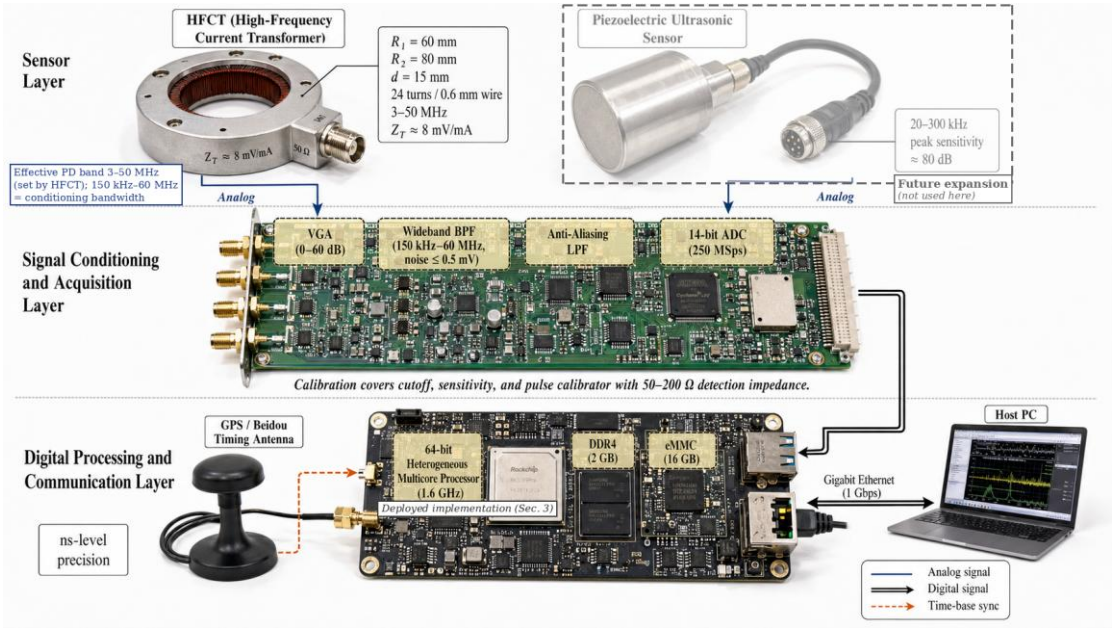

Fig. 1. Hardware architecture of the wideband HFCT-based partial discharge detection system. The piezoelectric ultrasonic channel is drawn as a future acoustic-fusion expansion only and is not used in this study

2.2 Characteristics of Pulse-Type Interference Signals

Three major interference types exist among pulse-type interferences that affect PD measurement in converter stations and UHV substations. The 12-pulse ripple produced by the thyristor-based system occurs every 1.67 ms (1/12th cycle of the fundamental period, 50 Hz). In the line-side winding bushing-tap, the pulses have a duration of around 200 μs, a rising edge of 3.9 to 4.24 μs, a pulse width of 80 to 83 μs, and an energy content within 99 percent at frequencies lower than 400 kHz and around a center frequency of 100 kHz. About 31 percent of the energy content in the bushing-tap signal is obtained relative to the neutral point signal energy content.

Corona interference pulse trains are found at the 90° and 270° phases of the power frequency cycle and consist of uniformly spaced pulses that exhibit a sharpness of about 287 ns with clear damped-oscillation trailing edges. Common examples are grounded conductors from core and clamp frames in 1000 kV substations with clear periodicity and uniformly spaced pulses. Switching interference consists of three pulse trains spaced at 120° phases with near-equal amplitudes for each. Individual pulses have rising edges that last about 13 ns and an overall spindle shape with distinct oscillations, similar to a distant discharge through power electronic devices.

The actual PD impulses registered under similar conditions vary across different parameters. The impulse edge occurs between 13 ns and 18 ns, the maximum amplitude occurs in the first peak, and the waveform is cone-shaped, which suggests proximity between the signal source and the receiver. In terms of void discharge interference, the impulse focuses on the first and third quadrants, with a concentration in the impulse number and varied amplitudes per impulse. This comparative analysis for the three types of interference is presented in Fig. 2.

Cumulative energy for the features is given by $E_T(t_k)$ and $E_F(f_k)$ in the time domain and frequency domain respectively, normalized with respect to the total energy, $E_T(t_k) = \frac{\sum_{i=1}^{k} x^2(t_i)}{\sum_{i=1}^{N} x^2(t_i)} \times 100\%$ and $E_F(f_k) = \frac{\sum_{i=1}^{k} |X(f_i)|^2}{\sum_{i=1}^{M} |X(f_i)|^2} \times 100\%$, where $x(t_i)$ is the sampled record of length N and $X(f_i)$ its M-point spectrum, on the basis that the short-time spectrum can extract the interfering signals from overlapping ones [20]. The instant at which E_T first exceeds 20% is regarded as the signal arrival

time and is used to adjust the time origin. The 20% level was selected from the laboratory records of Section 2.4: with a signal-free pre-trigger window, the cumulative energy of the noise floor grows approximately linearly and stays below 20% over the whole pre-trigger interval, whereas a PD or interference pulse raises E_T above this level within a few samples of its onset, so that the criterion corresponds to an energy step exceeding the noise contribution by more than three standard deviations of the pre-trigger cumulative energy. In addition, the oscillation ratio used for discrimination in Section 2.3 is defined as $R_{osc} = \frac{\sum_{n>n_z} x^2[n]}{\sum_n x^2[n]}$, where n_z is the first zero crossing after the main peak, i.e., the fraction of pulse energy contained in the trailing oscillation. Cone-shaped PD pulses concentrate their energy in the first peak and thus exhibit a low R_{osc}, whereas spindle-shaped electronic switching pulses and corona pulses with damped-oscillation tails exhibit a high R_{osc}; the value 0.6 lies between the two populations observed in the 220 kV laboratory records.

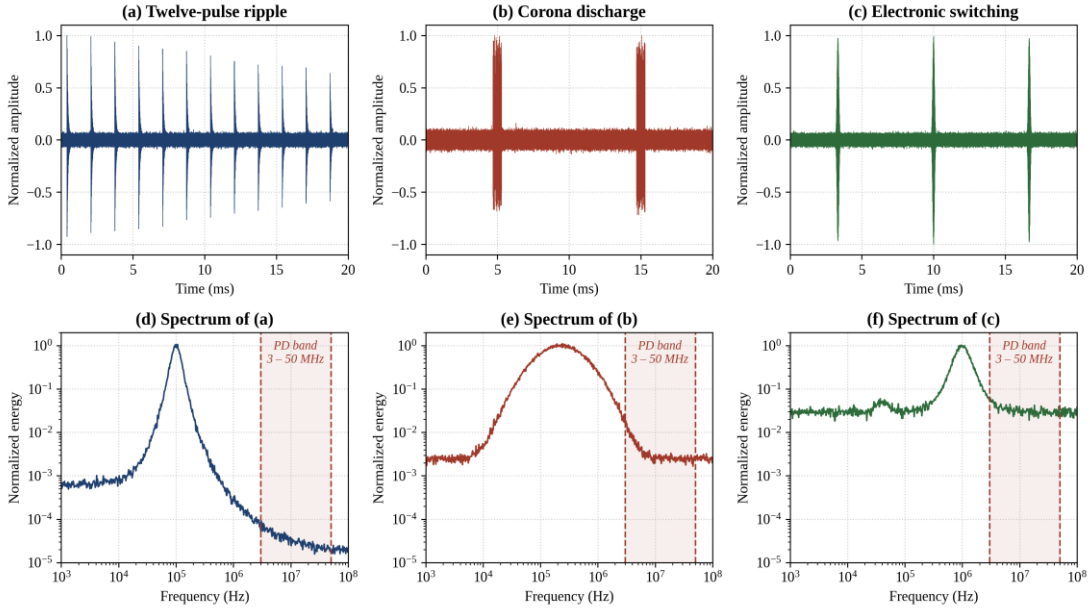

Fig. 2. Comparison of time-frequency characteristics of three typical pulse-type interference signals

2.3 Improved Wavelet Threshold Denoising Algorithm

Db5 wavelet from the family of Daubechies wavelets is chosen as the mother wavelet to extract PD coefficients since its damped sinusoidal shape approximates that of the PD pulses quite accurately, thus giving a highly correlated result between the inner products of the two and keeping the PD energy within a few detail coefficients only. Six levels of decomposition are used because higher-level decompositions diffuse the PD energy across the different approximation scales to a great extent, while lower-level decompositions leave broadband noise.

Hard thresholding assigns values less than λ to be zeros while keeping others the same; however, the point-wise non-smoothness at |w|=λ induces Pseudo-Gibbs effect in the reconstructed waveforms. Soft thresholding reduces each surviving value by exactly λ; hence, a residual magnitude bias is introduced, causing the first peak magnitude of the PD pulses to decay. A continuously differentiable thresholding scheme with a tunable factor $\alpha \in (0,1)$ is proposed. In the case of $|w| \geq \lambda$, the scheme tends to approach the original value by an exponentially diminishing bias with respect to α. Conversely, when $|w| < \lambda$, the scheme gradually diminishes towards zero. The function is continuous and differentiable at the critical value, thereby inhibiting the pseudo-Gibbs phenomenon linked to hard thresholding while simultaneously minimizing the constant error of soft thresholding. The proposed function is written separately for the two regions. For $|w| \geq \lambda$, $\hat{w} = sgn(w)(|w| - \alpha\lambda e^{-\frac{|w|-\lambda}{\lambda}})$; for $|w| < \lambda$, $\hat{w} = sgn(w)(1-\alpha)\lambda(\frac{|w|}{\lambda})^m$, with $m = \frac{1+\alpha}{1-\alpha}$, where w is a

detail coefficient, λ the layer threshold, $\hat{w}$ the thresholded coefficient, and $\alpha \in (0,1)$. Both expressions take the value $(1-\alpha)\lambda$ and the slope $1+\alpha$ at $|w|=\lambda$, so the function is continuous and continuously differentiable there; for $|w| \gg \lambda$ the bias $\alpha\lambda e^{-(|w|-\lambda)/\lambda}$ vanishes exponentially, and for $\alpha \to 1$ the function approaches soft thresholding while for $\alpha \to 0$ it approaches hard thresholding above λ. Threshold functions of this type have demonstrated significant improvements in waveform accuracy in stator PD noise removal applications [21].

The traditional universal threshold $\lambda = \sigma\sqrt{2lnN}$ presumes uniform noise variance in all the layers of the decomposition. As a result, there would be too much suppression of the low-frequency components and insufficient suppression of the high-frequency components during multi-level decomposition of the signal. Instead, layer-wise noise estimates are used here based on the median values of the detail coefficients within each respective layer j, $\sigma_j = \frac{median(|cD_j|)}{0.6745}$ and $\lambda_j = \sigma_j\sqrt{2lnN_j}$, where cD_j are the detail coefficients and N_j their number at level j. Higher thresholds will be assigned to high-frequency components, and vice versa, in compliance with the energy distribution of PD transients across different scales. Analogous approaches were experimentally justified in the case of wavelet-based denoising of physiologically generated transients [22].

The full workflow couples pulse pre-localization with waveform-level discrimination through six sequential steps. The noisy input is first passed into a cumulative energy function $E(i) = \sum_{k=1}^{i} x^2(k)$, whose maximum value identifies the position of the PD event, after which a windowed segment around that position is extracted. The segment is decomposed by db5 wavelet to six levels, producing detail coefficients cD1 through cD6 and approximation coefficients cA6. The layer-specific thresholds are computed for all the detail layers and employed via the advanced thresholding approach using α=0.5. The application of inverse wavelet transformation produces an intermediate denoised signal. This is followed by a discriminating phase where rising edge duration, signal slope, and oscillation ratio are compared to those values found in Sec. 2.2, resulting in the classification of all the pulses with a rising-edge duration longer than 200 ns or an oscillation ratio R_{osc} (Section 2.2) greater than 0.6 as interfering signals, while the others are considered valid PD pulses. The whole procedure is illustrated in Fig. 3.

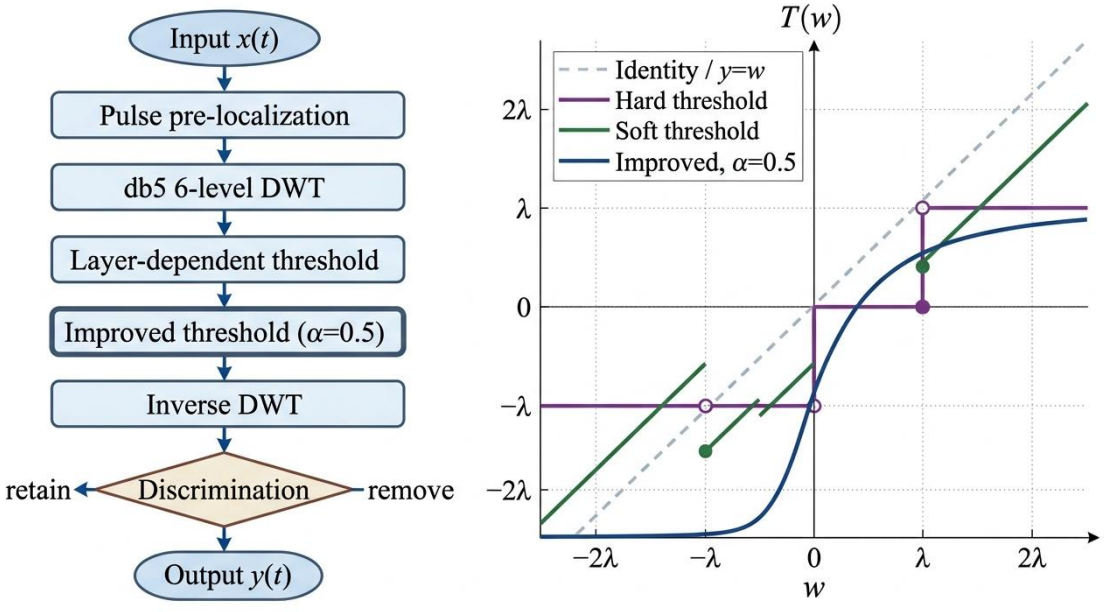

(a) Algorithm workflow (b) Threshold-function comparison

Fig. 3. Overall workflow of the improved wavelet threshold algorithm together with a comparison of the core threshold functions: (a) algorithm workflow; (b) comparison of the proposed continuously differentiable threshold function (α = 0.5) with the hard and soft threshold functions

2.4 Experimental Datasets and Denoising Evaluation Metrics

Three datasets with different degrees of realism are created to test the algorithms. In the first one, the synthesis of a PD pulse is carried out using Gaussian-2 and double-exponential (DEC) models, $x_{G2}(t) = A_1 e^{-(t-t_1)^2/(2\sigma_1^2)} - A_2 e^{-(t-t_2)^2/(2\sigma_2^2)}$ and $x_{DEC}(t) = A(e^{-t/\tau_1} - e^{-t/\tau_2})$, $t \geq 0$, with unit peak amplitude; the time constants (τ_1, τ_2, σ_1, σ_2) and peak spacing ($t_2 - t_1$) are drawn uniformly so that the 10%–90% rising edge falls within 13–18 ns and the pulse width within 50–200 ns, in accordance with the measured PD statistics in Section 2.2. For each synthesized PD pulse, interference pulses of the three types described in Section 2.2 along with additive Gaussian white noise are added. The ratio of the signal to noise varies from −5 to 15 dB at 2 dB intervals resulting in a total of 500 data samples.

Laboratory data set was obtained using a 220kV single-phase ultra-high voltage transformer simulation setup launched in 2025 with a capacity of 2MVA, having winding connection type of IiO and a short circuit impedance of 16.5%. The four classic models of defects, such as void discharge, surface discharge, floating electrode discharge, and tip discharge, were generated in the test tank, collecting 80 samples for each of them, thus totaling 320 data sets.

The field dataset consists of the collected measurements from three illustrative substations in 2025. The ±800 kV converter station in Xinjiang will supply the 12-pulse interference case from its converter transformer; the 1000 kV Ultra High Voltage substation in Nanyang, Henan Province, will be the source of the corona-dominated case under high reactor core and clamping frame grounding configuration; while the 500 kV substation main transformer supplies the compound interference case. There will be 60 samples retained for each case, thus totaling 180 samples for the entire field dataset. The field validation procedure follows the practice reported for on-site PD measurement [23].

Five parameters assess the denoising effectiveness. The noise reduction ratio $NRR = 10lg(\sigma_1^2/\sigma_2^2)$ describes the attenuation in decibels (dB) of noise variance from input to output, where σ_1 and σ_2 are the noise standard deviations before and after denoising. The energy retention ratio $ERR = \sum y^2/\sum x^2$ shows the proportion of energy that is maintained, where x is the original noisy input record and y the denoised output. The combined fitness $F = \sqrt{NRR \cdot ERR}$ provides a trade-off between the effectiveness of suppression and the preservation of the waveform; here the numerical value of NRR in dB is used, so that F is an empirical, dimensionless figure of merit (the geometric mean of a suppression score and a retention score) intended only for the relative ranking of methods and parameter settings, not a physical quantity. Normalized cross correlation $NCC = \frac{\sum x_c y}{\sqrt{\sum x_c^2 \sum y^2}}$ measures the similarity of the denoised wave y to the ideal clean wave x_c. Processing time for one record t is measured in milliseconds.

3. Results

3.1 Simulation Signal Denoising Performance

In order to analyze the efficiency of the new algorithm, the simulation dataset of 500 samples as discussed in section 2.4 was considered initially, keeping α=0.5, unless specified. With the variation of SNR from −5 dB to 15 dB, the SNR output increases continuously in accordance with the input SNR value. At −5 dB SNR, the output SNR obtained is 5.8 dB with an SNR improvement of 10.8 dB and NCC of 0.886. Increasing the input SNR to 0 dB gives SNR output of 9.6 dB with NCC=0.912. With an input of 5 dB, the output is 13.2 dB for an NCC of 0.937. When the input increases to 10 dB, the output is 17.8 dB for an NCC of 0.954, whereas, with the cleanest input of 15 dB, the output becomes 22.5 dB for an NCC of 0.968. The overall statistics, along with NRR, ERR, F, and per record processing time, are shown in Table 1 below.

At the reference input SNR of 5 dB (the center of the sweep, used hereafter as the representative operating point), the NRR value is 6.34 ± 0.42 dB, the ERR value is 0.89 ± 0.05, and the value of fitness function F is 2.38 ± 0.18; the corresponding values at the other SNR levels are listed in Table

1. The percentage of records with an NCC value greater than 0.92 is 88.4%, suggesting that good waveform similarity is maintained in most instances, instead of only when there is high input SNR.

Table 1. Statistical performance of the improved algorithm on 500 simulation samples (α = 0.5)

Input SNR (dB)	Output SNR (dB)	NRR (dB)	ERR	Combined fitness F	NCC	Processing time (ms)
−5	5.8 ± 0.6	7.12 ± 0.45	0.83 ± 0.07	2.43 ± 0.21	0.886 ± 0.031	50 ± 4.2
0	9.6 ± 0.5	6.85 ± 0.42	0.87 ± 0.06	2.44 ± 0.19	0.912 ± 0.027	51 ± 4.5
5	13.2 ± 0.5	6.34 ± 0.42	0.89 ± 0.05	2.38 ± 0.18	0.937 ± 0.024	52 ± 4.6
10	17.8 ± 0.6	5.91 ± 0.40	0.91 ± 0.04	2.32 ± 0.17	0.954 ± 0.020	53 ± 4.4
15	22.5 ± 0.7	5.42 ± 0.39	0.93 ± 0.03	2.24 ± 0.15	0.968 ± 0.016	53 ± 4.5

An investigation on the variable α shows its importance in adjusting from the hard mode to the soft mode. Setting α to 0.1 results in the hard-threshold mode and makes F decrease to 2.05, whereas setting α to 0.9 brings F up to 2.12 due to the soft-threshold mode. Maximum F (2.38) occurs when α = 0.5 and is located in between two opposite cases. In this condition, the edge recovery error and pulse-width recovery error, computed as the relative deviation of the 10%–90% rising-edge time and of the pulse width of the denoised pulse from those of the clean synthesized template (the rising-edge figure is also reported in Table 5), do not exceed 6.5% and 7.2%, respectively, which are acceptable in terms of engineering criteria for PRPD application.

The most insightful result is obtained for the case of low input SNRs. Specifically, the superior threshold function results in an improvement in output SNR of 2.4 dB at an input SNR of 0 dB and less compared to regular soft thresholding. This difference diminishes as the input SNR increases because the performance difference among the threshold functions decreases as the input becomes more pronounced than the noise.

3.2 Pulse-Type Interference Suppression in the Laboratory

The refined algorithm is then used on the 320 lab files; in each of the pulse interference types, the data is individually analyzed before the composite is formed, whereby the three cases are combined. When considering the 12-pulse scenario, ripple synchronized to a 1.67 ms cycle is added to the defect cell of the void discharge condition. Statistics from the output show that NRR = 6.18 dB, ERR = 0.92, and F = 2.38. The blind area for detection, represented by the ratio of cycles where PD signals cannot be isolated, decreases from 6.5 percent in the raw data to 2.85 percent post-processing. The result is close to the 2.31 percent threshold obtained in past experiments for twelve-pulse rejection systems, while the proposed framework encompasses corona discharge and electronic switching as well.

As for corona, pulses with steepness at 287 ns and oscillation tailing clearly defined are injected into phase points of 90° and 270°. The algorithm produces results of NRR = 5.92 dB, ERR = 0.91, and F = 2.32. The separation between PD pulses at 16 ns and corona pulses at 287 ns is based on the criterion of steepness, and the interference detection rate amounts to 93.6%. For the electronic switching case, spindle-like cluster pulses appear with phase separation at 120° and rising edges at 40 ns; the pulse recognition rate reaches 94.3%. For the combination case, the three kinds of interferences are introduced simultaneously, and the metrics stabilize to NRR = 5.65 dB, ERR = 0.86, and F = 2.20, where the PD identification rate is 91.2%, and it is more practical than the ideal result. Some sample waveforms prior to and after the processing are depicted in Fig. 4, and the combined suppression results are tabulated in Table 2.

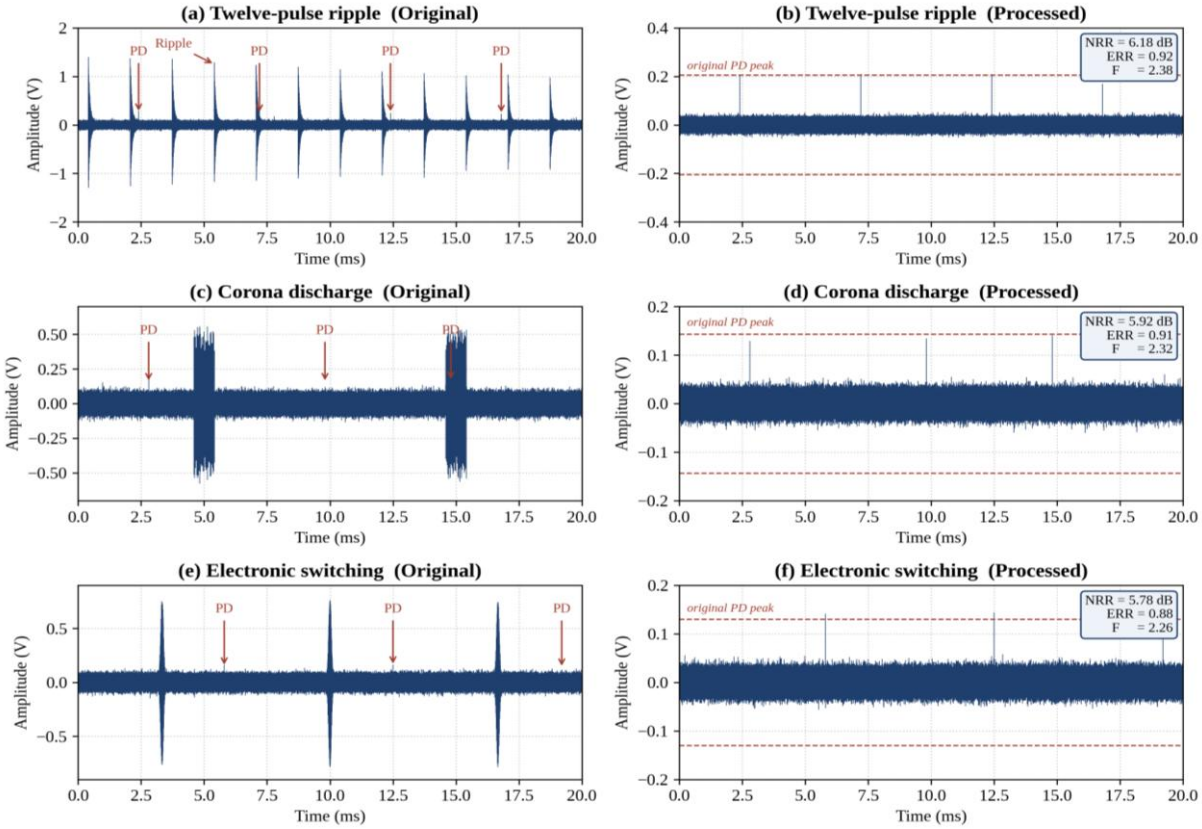

Fig. 4. Comparison of waveforms before and after denoising under three typical pulse-type interference scenarios on the 220 kV physical simulation platform: (a), (c), (e) original waveforms under 12-pulse ripple, corona, and electronic switching interference, respectively; (b), (d), (f) the corresponding processed waveforms. The vertical scale of the processed waveforms is zoomed in to clearly present the recovered nanosecond-level PD pulses after suppression of the high-amplitude interference; the red dashed lines in (b), (d), (f) mark the original PD peak amplitude for reference. Arrows labelled PD mark the partial discharge pulses and "Ripple" marks a 12-pulse ripple pulse in (a)

Table 2. Suppression performance for the three pulse-type interference categories under laboratory conditions.

Interference type	NRR (dB)	ERR	F	Identification rate (%)	Misjudgment rate (%)	Processing time (ms)
Twelve-pulse	6.18	0.92	2.38	95.2	2.85	49
Corona	5.92	0.91	2.32	93.6	4.10	53
Electronic switching	5.78	0.88	2.26	94.3	3.80	51
Composite	5.65	0.86	2.20	91.2	5.40	58

Table 3. Feature-parameter retention of the four canonical discharge defect signals after improved-algorithm processing

Defect type	Sample size	Mean NCC	Rising-edge error (%)	Pulse-width error (%)	First-peak retention (%)
Void discharge	80	0.943	5.8	6.4	94.1
Surface discharge	80	0.928	7.2	8.1	91.8
Floating-electrode discharge	80	0.952	4.6	5.9	95.3
Tip discharge	80	0.961	4.1	5.2	96.0

For the four defect models, NCC along with rising edge time error, pulse width error, and peak energy are used to represent waveform fidelity. The floating electrode and tip discharge have the highest NCC at 0.952 and 0.961, respectively, because their peak energies are highly concentrated and pass thresholding easily. The void and surface discharge models show NCC values of 0.943 and 0.928, respectively. For all the defect models, both the rising edge time and pulse width errors do not exceed 8.1%, while peak energy does not fall below 91%. The numerical breakdown is given in Table 3.

3.3 Field Validation on Three Substation Cases

The three datasets for the substations, as described in Section 2.4, are analyzed with identical parameters employed in the laboratory experiment, and the results are individually presented prior to their compilation. In the first instance (Case I), a transformer under test for a ±800 kV converter station in May 2025 produces raw data that include a distinct 1.67 ms periodic ripple alongside 12-pulse clusters whose leading edges fall close to 4.2 μs, while the potential partial discharges barely stand out against this background. Following post-processing, the ripple is filtered out, revealing a clean partial discharge with an 18 ns rising edge, achieving a peak preservation rate of 93.2%. Under 0.8 U_0 stimulation, a void discharge is detected at an apparent charge value close to 1053 pC against the background signal, matching the manually measured value in the initial commissioning document. A discharge of this magnitude far exceeds the acceptance level for a converter transformer and indicates an active insulation defect; the unit was therefore withheld from energization and returned for defect location and repair before the acceptance test was repeated. The processing time per record is 52 ms.

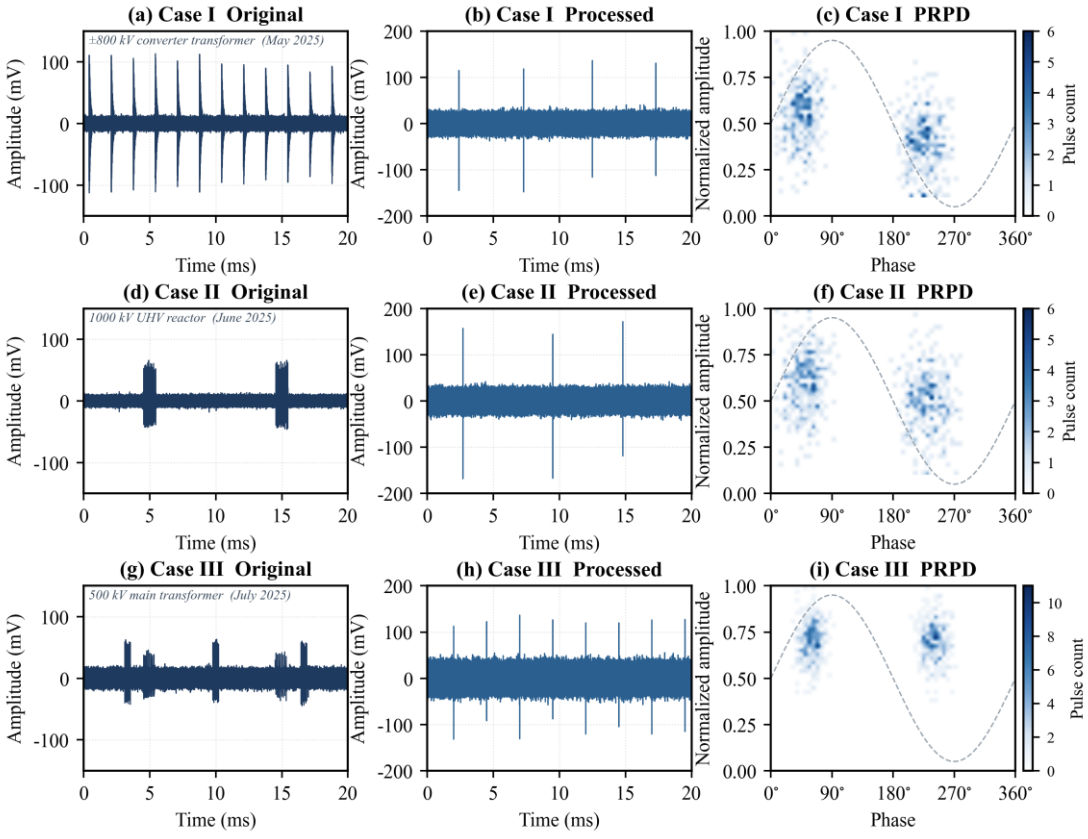

Fig. 5. Field validation of the algorithm on three representative substation cases. Rows correspond to cases I to III; columns show the original waveform, the processed waveform, and the PRPD pattern

The second sample comes from a 1000 kV UHV HV shunt reactor in June 2025. The initial raw signal from the center and the grounding lead of the clamping frame contains strong periodic corona discharges located at 90° and 270° with steepness of about 287 ns and prominent tailing oscillations, along with small PDs at the first and third quadrants. Following the data processing,

the corona discharge components are eliminated, and the signal at 16 ns and approximately 225 mV can be seen in the expected quadrants, which suggests void discharge initially. The maximum errors for feature parameters at the grounding location are below 5%.

The third example refers to a 500 kV power transformer measured in July 2025. The input signal with an applied voltage of 246 kV contains considerable interference from both external and internal sources, including white noise, corona discharges, and switching pulses. In this scenario, the proposed algorithm successfully filters a floating electrode discharge pulse of 3540.9 pC, showing symmetrical and periodic behavior in the first and third quadrants. The ns-level time-difference analysis across the synchronized HFCT channels (Section 2.1) reveals that the bushing-tap signal leads the remaining channels by 25–51 ns, which places the source at the bottom end of the high-voltage bushing. This location was confirmed by subsequent physical inspection, which traced the fault to the connection bolt of the corona ring assembly. A floating-electrode discharge above 3500 pC represents a severe and potentially escalating defect; the transformer was consequently de-energized, and the loose bolt was re-tightened and the assembly inspected before the unit was returned to service, after which the discharge disappeared. On average over all 180 field records, the detection accuracy is 93.7% with an overall misdiagnosis ratio of 3.5% (the higher 5%–8% figure discussed in Section 4.2 refers only to the subset of near-field pulses), and the parameter reconstruction error is within 8%. Time-domain and PRPD comparisons are shown in Fig. 5, and the consolidated case-level metrics are listed in Table 4.

Table 4. Summary of algorithm performance on the three field cases

Case	Site	Dominant interference	Test date	Detected PD type	NRR (dB)	First-peak retention (%)	Detection accuracy (%)	Processing time (ms)
I	±800 kV converter station, converter transformer	Twelve-pulse	2025.05	Void discharge	6.05	93.2	94.5	52
II	1000 kV UHV station, high-voltage reactor	Corona	2025.06	Void discharge	5.83	91.6	92.8	54
III	500 kV substation, main transformer	Composite	2025.07	Floating-electrode discharge	5.71	90.4	93.7	57
Pooled	/	/	/	/	5.86	91.7	93.7	54.3

Note: Pooled metrics are equal-weight averages of the three cases (N = 60 records per case, total N = 180).

3.4 Comparison with Conventional Denoising Methods

The enhanced algorithm is compared to four existing algorithms, which are the adaptive SVD, EMD coupled with wavelet thresholding, and both the hard and soft thresholds techniques. All five techniques were tested using the same 500-element simulated dataset with equivalent mother-wavelet, decomposition level, and SNR sweeps, and means were calculated from all datasets. SNR output enhancement for the proposed method amounts to 9.3 dB, in comparison to 8.5 dB, 7.8 dB, 7.1 dB, and 6.2 dB respectively for the other four algorithms. Waveform accuracy is consistent with the above results: the NCC measures for the proposed approach is 0.91, while the NCC for the other approaches remains 0.87, 0.85, 0.83, and 0.78, respectively. Performance on 1024 samples data differs. The enhanced algorithm requires only 52 ms compared to the 38 ms required by hard thresholding and 41 ms required by soft thresholding but significantly faster than the 420 ms for EMD-thresholding and 185 ms for adaptive SVD. The percentage improvement in speed is 87.6% for EMD-thresholding and 71.9% for adaptive SVD. The extra time taken (approximately 25%) for enhanced algorithms yields a 13.3% improvement in total fitness F over hard thresholding and a 15.0% improvement over soft thresholding. The six-dimensional comparison is shown in Fig. 6, in

which each metric is normalized to its maximum across the five methods (range 0–1) and the raw value is annotated above each bar; the computational efficiency score is defined as $\eta_c = t_{min}/t$, with t_{min} the shortest processing time among the five methods; and the consolidated metrics are listed in Table 5.

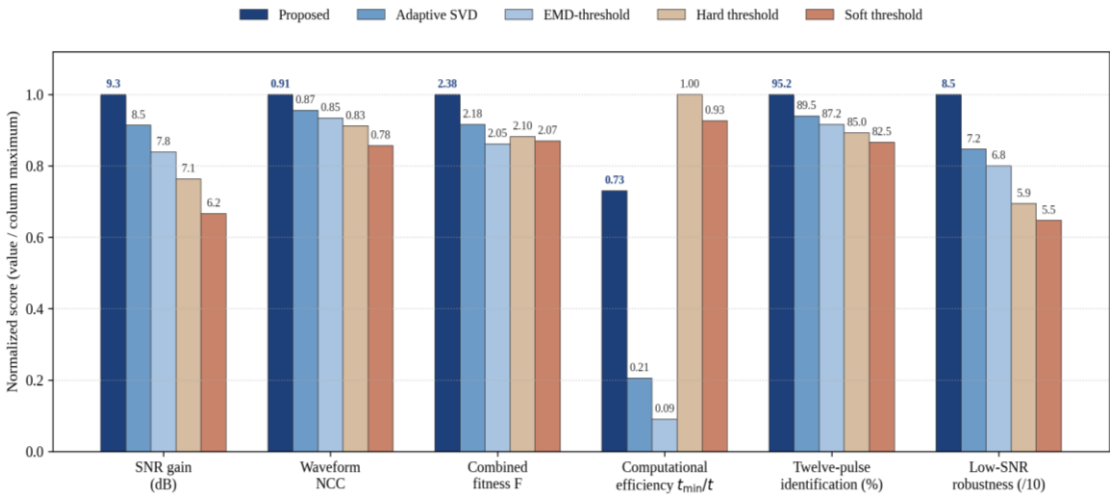

Fig. 6. Multi-dimensional bar-chart comparison of five denoising methods on the simulation dataset (each metric normalized to its column maximum; raw values from Table 5 annotated above the bars; computational efficiency = t_{min}/t)

Table 5. Performance comparison of five denoising methods (mean values across 500 simulation samples)

Metric	Proposed	Adaptive SVD	EMD-threshold	Hard threshold	Soft threshold
SNR gain (dB)	9.3	8.5	7.8	7.1	6.2
Waveform NCC	0.91	0.87	0.85	0.83	0.78
Combined fitness F	2.38	2.18	2.05	2.10	2.07
Processing time (ms)	52	185	420	38	41
Twelve-pulse identification rate (%)	95.2	89.5	87.2	85.0	82.5
Rising-edge retention error (%)	6.5	8.7	10.2	7.8	12.6
Robustness score (−5 dB to 15 dB)	8.5 / 10	7.2 / 10	6.8 / 10	5.9 / 10	5.5 / 10

Collectively, the advanced algorithm beats all four of the thresholding strategies on the first three out of the five performance criteria, specifically the SNR enhancement factor, waveform preservation, and the percentage of twelve-pulses detected, while the rising-edge error remains below the 8% threshold. While the traditional thresholding schemes enjoy better execution time for noise-free signals, their maximum achievable SNR and waveform preservation levels are severely degraded when pulse-type noises exist in the signal, in line with Section 3.2's experimental findings. EMD-threshold and adaptive SVD can fill in some of the SNR loss compared to thresholding schemes, but the computational overhead of each sample makes integration into a 250 MSps stream impossible. Hence, the novel design is in an optimal position between efficiency and accuracy, providing multi-tens-of-milliseconds latency and achieving SNR and NCC values only partially attained by baseline solutions.

4. Discussion

4.1 Stability of the Improved Threshold Function

Another interesting aspect that needs exploring is the sensitivity of the algorithm to the factor α. When α varies within the range of 0.3 to 0.7, F remains in a margin of 8 percent (2.18 < F < 2.38). The best value for α is 0.5, which occurs in the middle of the gradual shift between the hard and soft cases, in agreement with the continuous derivative nature seen in Fig. 3. This indicates that minor changes in α have little effect on the results, making it easier to control the parameters used in practice [24].

The case of SNR adaptive range follows suit. For the −5 dB to 15 dB range examined in Section 3.1, the ratio deviation is less than 12% of the average of the NRR, implying that the layer-based threshold estimation remains highly stable and robust despite any level of contamination. This phenomenon conforms to results of optimization-based wavelet-based denoising of nonstationary power system signals where threshold adaptation exhibited stability at different SNR values [25]. The dependence of the mother-wavelet choice on the noise source reported in PD denoising [26].

The two design decisions that provide this robustness are first, the use of a continuously differentiable threshold function that gets rid of the discontinuity at |w|=λ and the pseudo-Gibbs ringing effect of hard thresholding, and second, using the estimator based on layer-specific variance estimates for the detail layers. They complement each other in a way that each cannot do alone, with the former preserving waveform shape and the latter avoiding over-suppression or under-suppression at a single scale. It is their joint action that makes possible the bounded variation of the metric values over α and SNR.

4.2 Adaptability Across Interference Types

Pulse-types fall under three classifications, each of which has varying degrees of difficulty in recognition. The first type is the twelve-pulse ripple with a success rate of 95.2%. This is because this type has a periodicity of 1.67 ms and a rise time in the microsecond range. These characteristics are quite distinct from the nanosecond-range rise time characteristic of PD. Using either the time domain steepness test or phase periodicity is sufficient to identify the twelve-pulse pulse-type.

The next classification is the corona interference type at 93.6%. In this case, the difference in steepness between the 287 ns corona and the 16 ns PD becomes sufficiently significant to separate them by means of the steepness threshold and oscillation criterion. Some rare pulses of low-intensity corona interference that have been transferred via the winding show a steepness value similar to those of the remote PDs, and these are the situations in which errors can take place. The technique of SVD-based spectrum subtraction has been proposed as an additional step in this case [27].

The third category is electronic switching interference, identified at 94.3% under laboratory conditions (Table 2). Recognition becomes harder once the three categories are superimposed: the PD identification rate of the composite laboratory case drops to 91.2% (Table 2), and in the corresponding composite field case (Case III) the detection accuracy is 93.7% (Table 4), the field records containing a more diverse set of switching sources than the laboratory setup. The phase pattern of 120° and the spindle envelope lead to the differentiation, despite the transient signals produced by switching close to the source having extremely sharp leading edges that come quite close to the PD levels [28]. The composite method is based on the cooperative effect between cumulative energy pre-localization and wavelet domain thresholding, where pre-localization extracts the candidate window while thresholding removes the residual broadband component. The other issue that persists is the presence of near-field pulses with waveform similar to PD, where misclassification within this subset can still occur between 5% and 8% (compared with the overall field misdiagnosis ratio of 3.5% in Section 3.3), and multichannel time of arrival fusion, coupled with hybrid wavelet-machine learning routing, could be a logical progression [29].

4.3 Computational Efficiency and Engineering Applicability

Real-time performance comes as the first requirement. When sampling at a frequency of 250 MSps, each acquired 20 ms power-cycle record takes 52 ms to process with our approach, fitting into the 100 ms update interval and allowing room for buffer management and generation of the PRPD pattern afterwards. It should be stated explicitly that the platform therefore operates in a buffered, duty-cycled mode rather than in gap-free acquisition: one 20 ms record is captured and processed per 100 ms update interval, i.e., a temporal coverage of 20%. Because PD assessment via PRPD patterns is statistical over many cycles, and because the pilot deployments (Section 4.3) showed that this coverage was sufficient to reduce the detection blind zone to 2.5%–3%, the mode is adequate for online condition assessment; nevertheless, it does not capture every power cycle, and gap-free acquisition would require pipelined processing on the FPGA implementation discussed below (Section 4.4). In comparison, the performance is much better than those of EMD-threshold (420 ms) and adaptive SVD (185 ms) from Section 3.4, matching the latency range found for hybrid wavelet-TV processing of PD signals [30].

The second issue concerns hardware portability. It can be easily stated that all basic computations carried out in the pipeline, which are wavelet decompositions of up to six levels, thresholding using the enhanced procedure, and calculation of total energy, are well suited to an embedded implementation on an FPGA+DSP platform. A synthesis study of the pipeline (not yet field-deployed; the results in Section 3 were obtained on the multi-core processor described in Section 2.1) indicates utilization of roughly 65% LUT resources and 42% BRAM resources for a mid-range FPGA device (Xilinx Artix-7 XC7A200T). Both these numbers lie below the saturation threshold, and they are on par with SVD PD denoising chains on similar hardware [31].

The feedback from field pilot tests reinforces the laboratory results. The detection blind area under high levels of interference reduced from a range of 6-8% to 2.5-3%, for the ±800kV converter station of Xinjiang, 1000kV ultra-high voltage substation in Nanyang, Henan province, and the 500kV main transformer site. The detection rate of PD pulses improved by about 15.3% against the pre-installation benchmark, facilitating early detection of insulation faults at commissioning and periodic maintenance phases.

4.4 Limitations and Future Work

There are several limitations that restrict the results obtained here. The study focuses mainly on the pulse current signals measured using the HFCT technique; however, the effectiveness of the proposed approach for ultrasound acoustic emission is yet to be confirmed using similar field measurements, considering the differences in the statistics of the noise channels and paths between the acoustics and the electrical front end. The adjustable parameter α is set to 0.5 as the empirically optimized value from the simulation sweep presented in Section 3.1, and has not been adapted on a per-record basis. The performance below the −5 dB lower bound of the investigated SNR range has not been characterized. Furthermore, the present platform acquires one 20 ms record per 100 ms update interval (Section 4.3), so PD events falling in the unrecorded intervals are not captured. The ability to adapt to novel interference types due to newly developed power electronic devices is constrained by the low quantity of such data in the current field database.

A number of approaches will be pursued to mitigate these limitations. First, the pipeline will be extended towards an implementation of acoustic-electric fusion through the coupling of the method described above with ultrasonic noise reduction and total variation autoencoders designed specifically for acoustic PD [32]. Second, particle swarm optimization will be used to automatically select α for each record. The third focuses on the combination between the optimized wavelet threshold approach with deep neural networks such as autoencoders and adaptive iterative filtering combined with the Bidirectional Long Short-Term Memory model [33]. Fourthly, the expanded database takes account of new forms of interfering noise from pulsating sources, and the results are linked to future localization[34] and recognition of PRPD patterns[35]. Thus, the benefits of increased waveform accuracy are transferred into the diagnostic decision-making process.

5. Conclusions

The engineering problem targeted in this research effort relates to the inability to detect partial discharges due to pulse-type interference in UHV transformer systems. An innovative technique for suppressing pulse-type interference through the use of an enhanced wavelet threshold has been invented, and is incorporated into a wideband detection system featuring a 150 kHz to 60 MHz signal conditioning bandwidth coupled with a 3–50 MHz high-frequency current transformer (HFCT) sensor, to create a fully-fledged signal-processing decision-making chain.

Regarding methodology, a continuously differentiable threshold function with a variable parameter α has been devised, which maintains the robust nature of hard thresholding while incorporating the smoothness of soft thresholding, without inheriting their limitations. An adaptive threshold value estimation scheme dependent upon a particular layer is adopted in lieu of the universal threshold scheme that has the tendency of over-sensing or under-sensing at low-frequency and high-frequency layers respectively when using multiresolution decomposition. The preprocessing of pre-localization and discrimination using time-frequency cumulative energy schemes enables the algorithm to reliably detect true PD events prior to thresholding.

In terms of results, the performance of the simulation data set is demonstrated by an average SNR improvement of 9.3 dB and a fitness F value of 2.38 at 5 dB input SNR, surpassing the values for EMD threshold (7.8 dB, F=2.05) and adaptive SVD (8.5 dB, F=2.18). In addition, all four standard defects in the lab data set possess an NCC value exceeding 0.92. The laboratory identification rates for the three interference classes are 95.2%, 93.6% and 94.3% respectively (Table 2); the field data yield an average detection accuracy of 93.7%, and feature parameter errors stay within 8.1%. The single data record processing time averages at 52 ms, satisfying the <100 ms online update requirement in a buffered, duty-cycled acquisition mode.

Value for engineering in regard to the three pilot installations at ±800 kV converter station, 1000 kV UHV substation, and 500 kV main transformer installation involved reducing the PD blind detection zone from 6%-8% to 2.5%-3%. In addition, the percentage of PD pulse detection was increased by 15.3% as compared to before the pilot installations. These results provide a functional means of analysis for engineers operating under conditions of high interference and enable more accurate assessment of the insulation condition of grid equipment. Future work will focus on extending this algorithmic approach to hybrid acoustic-electric interference removal, runtime optimization of α, and integration of deep learning models, the overall goal being to increase generalizability toward new sources of pulse-based interference in power electronics.

Reference

[1] Sikorski W, Wielewski A. Low-cost online partial discharge monitoring system for power transformers. Sensors. 2023;23(7):3405. https://doi.org/10.3390/s23073405

[2] Sikorski W, Gielniak J. Online monitoring of partial discharges in large power transformers using ultra-high frequency and acoustic emission methods: case studies. Energies. 2025;18(7):1718. https://doi.org/10.3390/en18071718

[3] Mwinisin P, Mingotti A, Peretto L, Tinarelli R, Tefferi M. Electrical diagnosis techniques for power transformers: a comprehensive review of methods, instrumentation, and research challenges. Sensors. 2025;25(7):1968. https://doi.org/10.3390/s25071968

[4] Tenbohlen S, Beura CP, Sikorski W, Albarracín Sánchez R, de Castro BA, Beltle M, et al. Frequency range of UHF PD measurements in power transformers. Energies. 2023;16(3):1395. https://doi.org/10.3390/en16031395

[5] Khamlichi A, Garnacho F, Simón P. New synthetic partial discharge calibrator for qualification of partial discharge analyzers for insulation diagnosis of HVDC and HVAC grids. Sensors. 2023;23(13):5955. https://doi.org/10.3390/s23135955

[6] Yang D, Zhang W, Xu G, Li T, Shen J, Yue Y, et al. Partial discharge pulse segmentation approach of converter transformers based on higher order cumulant. Energies. 2022;15(2):415. https://doi.org/10.3390/en15020415

[7] Carvalho IF, da Costa EG, Nobrega LAMM, Silva ADdC. Identification of partial discharge sources by feature extraction from a signal conditioning system. Sensors. 2024;24(7):2226. https://doi.org/10.3390/s24072226

[8] Shams MA, Anis HI, El-Shahat M. Denoising of heavily contaminated partial discharge signals in high-voltage cables using maximal overlap discrete wavelet transform. Energies. 2021;14(20):6540. https://doi.org/10.3390/en14206540
[9] Dhandapani R, Mitiche I, McMeekin S, Sarma Mallela V, Morison G. Enhanced partial discharge signal denoising using dispersion entropy optimized variational mode decomposition. Entropy. 2021;23(12):1567. https://doi.org/10.3390/e23121567
[10] Yang J, Yan K, Wang Z, Zheng X. A novel denoising method for partial discharge signal based on improved variational mode decomposition. Energies. 2022;15(21):8167. https://doi.org/10.3390/en15218167
[11] Zhong J, Liu Z, Bi X. Partial discharge signal denoising algorithm based on Aquila optimizer–variational mode decomposition and k-singular value decomposition. Appl Sci. 2024;14(7):2755. https://doi.org/10.3390/app14072755
[12] Wu Z, Zhang Z, Zheng L, Yan T, Tang C. The denoising method for transformer partial discharge based on the whale VMD algorithm combined with adaptive filtering and wavelet thresholding. Sensors. 2023;23(19):8085. https://doi.org/10.3390/s23198085
[13] Wang H, et al. Enhanced noise suppression in partial discharge signals via SVD and VMD with wavelet thresholding. Modelling and Simulation in Engineering. 2024:5676986. https://doi.org/10.1155/2024/5676986
[14] Chen B, Li K, Guo Y. Effective denoising of multi-source partial discharge signals via an improved power spectrum segmentation method based on normalized spectral kurtosis. Sensors. 2025;25(12):3798. https://doi.org/10.3390/s25123798
[15] Cao J, Wang Y, Zhu W, Zhang Y. A noise reduction algorithm for white noise and periodic narrowband interference noise in partial discharge signals. Appl Sci. 2025;15(4):1760. https://doi.org/10.3390/app15041760
[16] Chen L, Wen Y, Su H, Xiong K, Chen D. Research on partial discharge signal recognition and classification of power transformer based on acoustic-VMD and CNN-LSTM. PLoS One. 2025;20(11):e0335447. https://doi.org/10.1371/journal.pone.0335447
[17] Wang Y, Zhu Y. Deep residual shrinkage network recognition method for transformer partial discharge. Electronics. 2025;14(16):3181. https://doi.org/10.3390/electronics14163181
[18] Fu Z, Wang Y, Zhou L, Li K, Rao H. Partial discharge recognition of transformers based on data augmentation and CNN-BiLSTM-attention mechanism. Electronics. 2025;14(1):193. https://doi.org/10.3390/electronics14010193
[19] Besharatifard H, Hasanzadeh S, Muyeen SM, Kamwa I. Evaluation of a calibration technique in measuring partial discharges inside mineral oils with a high-frequency current transformer (HFCT) sensor: a case study. IET Gener Transm Distrib. 2023;17(3):706-715. https://doi.org/10.1049/gtd2.12699
[20] Tao Z. Narrowband interference suppression of partial discharge based on short-time Fourier transform. Proc CSEE. 2022;45(4):11-15.
[21] Yang D, Song K, Yi R, Xiong H, Yang X. Denoising of partial discharge signal in stator using wavelet transform with improved thresholding function. Appl Sci. 2025;15(19):10509. https://doi.org/10.3390/app151910509
[22] Zhang Y, Yu K, Huang C, Qu R, Fan Z, Zhu P, et al. Adaptive layer-dependent threshold function for wavelet denoising of ECG and multimode fiber cardiorespiratory signals. Sensors. 2025;25(24):7644. https://doi.org/10.3390/s25247644
[23] Cao T, Cui Y, Tan H, Lu W, Zhang F, Liu K, et al. A field verification denoising method for partial discharge ultrasonic sensors based on IPSO-optimized multivariate variational mode decomposition combined with improved wavelet transforms. Sensors. 2025;25(24):7506. https://doi.org/10.3390/s25247506
[24] Goh HH, et al. Denoising transient power quality disturbances using an improved adaptive wavelet threshold method based on energy optimization. Energies. 2022;15(9):3081. https://doi.org/10.3390/en15093081
[25] Akkaya S. Wavelet-based denoising strategies for non-stationary signals in electrical power systems: an optimization perspective. Electronics. 2025;14(16):3190. https://doi.org/10.3390/electronics14163190
[26] Sahnoune MA, Zegnini B, Seghier T, Flah A, Kanan M, Prokop L, et al. Noise source effect on the quality of mother wavelet selection for partial discharge denoising. IEEE Access. 2024;12:132729-132743. https://doi.org/10.1109/ACCESS.2024.3459474
[27] Xu Y, Jing Y, Wang Y, He R, Wang J, Geng Y. Novel denoizing method for partial discharge signals using singular value decomposition and spectral subtraction. IET Sci Meas Technol. 2023;17(3):105-114. https://doi.org/10.1049/smt2.12134
[28] Rodrigo-Mor A, Muñoz FA, Castro-Heredia LC. Principles of charge estimation methods using high-frequency current transformer sensors in partial discharge measurements. Sensors. 2020;20(9):2520. https://doi.org/10.3390/s20092520

[29] Chen S, Illias HA, Wong JKR, Mansor NN. Denoising of partial discharges in switchgear insulation material using hybrid wavelet denoising-optimization-machine learning. Ain Shams Eng J. 2024;15(11):103032. https://doi.org/10.1016/j.asej.2024.103032
[30] Tang J, Zhou S, Pan C. A denoising algorithm for partial discharge measurement based on the combination of wavelet threshold and total variation theory. IEEE Trans Instrum Meas. 2019;69(6):3428-3441. https://doi.org/10.1109/TIM.2019.2938905
[31] Govindarajan S, Subbaiah J, Cavallini A, Krithivasan K, Jayakumar J. Development of Hankel-SVD hybrid technique for multiple noise removal from PD signature. IET Sci Meas Technol. 2019;13(8):1075-1084. https://doi.org/10.1049/iet-smt.2018.5679
[32] Chaudhuri S, Ghosh S, Dey D, Munshi S, Chatterjee B, Dalai S. Denoising of partial discharge signal using a hybrid framework of total variation denoising-autoencoder. Measurement. 2023;223:113674. https://doi.org/10.1016/j.measurement.2023.113674
[33] Shang H, Zhao Z, Zhang R, Wang Z, Li J. Transformer partial discharge fault diagnosis based on improved adaptive local iterative filtering-bidirectional long short-term memory. IET Electr Power Appl. 2024;18(10):1214-1232. https://doi.org/10.1049/elp2.12471
[34] Khodaveisi F, Karami H, Karimpour MZ, Rubinstein M, Rachidi F. Partial discharge localization in power transformer tanks using machine learning methods. Sci Rep. 2024;14:11785. https://doi.org/10.1038/s41598-024-62527-9
[35] Abubakar A, Zachariades C. Phase-resolved partial discharge (PRPD) pattern recognition using image processing template matching. Sensors. 2024;24(11):3565. https://doi.org/10.3390/s24113565
[36] CIGRE Working Group A2.37. Transformer reliability survey. CIGRE Technical Brochure 642. Paris: CIGRE; 2015. https://www.e-cigre.org/publications/detail/642-transformer-reliability-survey.html